

4D iRIOM: 4D Imaging Radar Inertial Odometry and Mapping

Yuan Zhuang¹, Senior Member, IEEE, Binliang Wang¹,
Jianzhu Huai^{1*}, Member, IEEE, Miao Li¹, Senior Member, IEEE

Abstract—Millimeter wave radar can measure distances, directions, and Doppler velocity for objects in harsh conditions such as fog. The 4D imaging radar with both vertical and horizontal data resembling an image can also measure objects' height. Previous studies have used 3D radars for ego-motion estimation. But few methods leveraged the rich data of imaging radars, and they usually omitted the mapping aspect which is affected by the radar multipath returns, thus leading to inferior odometry accuracy. This paper presents a real-time imaging radar inertial odometry and mapping method, iRIOM, based on the submap concept. To fend off moving objects and multipath reflections, the iteratively reweighted least squares method is used for getting the ego-velocity from a single scan. To measure the agreement between sparse non-repetitive radar scan points and submap points, the distribution-to-multi-distribution distance for matches is adopted. The ego-velocity, scan-to-submap matches are fused with the 6D inertial data by an iterative extended Kalman filter to get the platform's 3D position and orientation. A loop closure module is also developed to curb the odometry module's drift. To our knowledge, iRIOM based on the two modules is the first 4D radar inertial SLAM system. On our and third-party data, we show iRIOM's favorable odometry accuracy and mapping consistency against the FastLIO-SLAM and the EKFRIO. Also, the ablation study reveal the benefit of inertial data versus the constant velocity model, the scan-to-submap matching versus the scan-to-scans matching, and loop closure.

Index Terms—4D imaging radar, radar inertial odometry and mapping, scan-to-submap, iterative EKF.

I. INTRODUCTION

Autonomous vehicles and robotics are developing rapidly in recent years. Positioning and navigation technology based on sensor fusion has been a popular research direction in this field. Currently, most platforms use lidars and cameras as primary sensors. These sensors have good performance in good weather, but struggle to work in degraded environments such as rain and fog [1]. The millimeter wave radar typically has a longer wavelength and a larger detection range, and is barely susceptible to small particles such as fog and rain [2]. Moreover, it can provide Doppler velocity observations, leading to ego-velocity from a single radar scan [3].

Compared to 3D radars, the 4D imaging millimeter wave radar greatly improves the resolution in the vertical direction, thus providing four types of information: distance, azimuth, height, and velocity. It allows better obstacle detection, ego-motion estimation, and path planning [4]. However, a 4D millimeter wave radar obtains scans of sparse point clouds

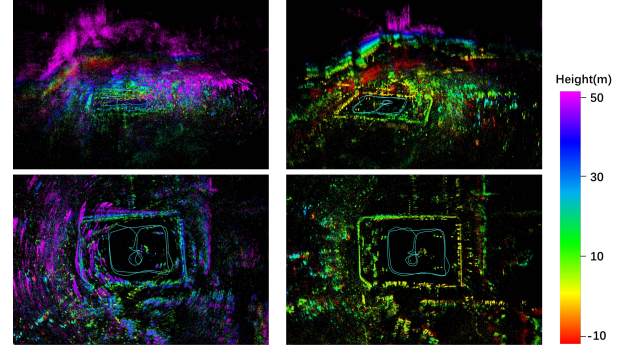


Fig. 1. Mapping results by iRIOM on data of a basketball court. Radar ego-velocity and IMU data are used for the left plots, and radar point matches are further added for the right plots. The blue curves are the estimated trajectories. Map points are colored by the elevation.

which are lower in spatial resolution than camera images or lidar scans at the moment. Moreover, radar scans suffer from multipath effects, harmonics and other noises, making it difficult to achieve reliable data association [5]. Thus, it is a challenging task to attain precise 3D localization and mapping by a 4D millimeter wave radar.

We propose an imaging radar inertial odometry and mapping method (iRIOM) using radar scans of point clouds and 6D IMU (inertial measurement unit) data. The iRIOM fuses ego-velocity from radar scans and scan-to-submap matches with IMU data to get accurate odometry and consistent mapping.

The main contributions of this paper are:

1. We fuse IMU data with ego-velocity from a radar scan and radar point matches by an iterative Kalman filter, forming a robust odometry and mapping system. In estimating ego-velocity, moving objects and multipath returns are suppressed by an iterative reweighted least squares method. The system were tested on indoor and outdoor sequences of our dataset and the ColoRadar dataset [6], showing good performance.
2. Instead of scan-to-scan matching [7], we use the scan-to-submap matching concept and design a distribution-to-multi-distribution point matching metric. This is tailored for the sparse radar points which often have no exact point matches, and reduces the trajectory drift of inter-frame matching. The advantages were validated with ablation studies.
3. We refine the poses from the radar odometry with loop closures to remove odometry drift and achieve consistent mapping. Our ablation study showed the consistent mapping results and the benefit of loop closure. To our knowledge, iRIOM is the first 4D imaging radar simultaneous localization

*Corresponding author: Jianzhu Huai

¹State Key Laboratory of Information Engineering in Surveying, Mapping, and Remote Sensing, Wuhan University, China

and mapping (SLAM) system with consistent mapping.

The rest of this paper is organized as follows. Section II reviews the related work on radar odometry and radar inertial odometry. Section III describes our proposed 4D radar inertial odometry method. Then, we experimentally validate the proposed method and analyze the results in Section IV. In Section V, we summarize the paper and draw conclusions.

II. RELATED WORK

We briefly review related work on 3D radar odometry, 4D radar inertial odometry, and radar-based place recognition.

A. 3D Radar Odometry

Conventional millimeter wave radars can only estimate planar position based on distance and azimuth data, and cannot get object heights due to the low elevation resolution. Thus, most radar odometry methods convert radar data to planar images or 2D point clouds, and then estimate odometry using image or point cloud matching methods. Based on the data association, these odometry methods can be grouped into feature-based and direct methods.

The feature-based approach first extracts key points and feature descriptors, and then associates key points by nearest neighbor searching in the feature space or graph matching without descriptors. Cen et al. [8], [9] proposed two radar key point detection methods, and showed that the two methods can suppress multipath noise and improve robustness of sequential radar scan matching. Aldera et al. [10] trained a focus of attention policy by a weakly supervised learning approach to down-sample the point clouds as preprocessing, reducing the time consumption while ensuring accuracy of the radar odometer. Barnes et al. [11] proposed a self-supervised radar key point detection and feature description network to generate good key point locations and descriptors for scan matching, which substantially improved accuracy of radar odometry. Hong et al. [12] used classical feature point detection and description algorithms (e.g., SURF) to associate adjacent scans to achieve pose estimation as the front end of a radar SLAM system, and used loop detection for global pose optimization. Burnett et al. [13] used the key point extraction and description algorithm proposed in [9] to build a radar SLAM system and considered motion distortion in the rotating radar data.

The direct methods estimate the relative pose by directly registering radar scans. Park et al. [14] proposed a direct radar odometry method by applying the Fourier-Melling transform (FMT) to estimate rotations and translations between sequential radar scans. In [15], Barnes et al. proposed a fully microscopic, correlation-based end-to-end radar odometry, where a mask network was trained to remove radar data noise, and the fast Fourier transform (FFT) matching method was used to obtain the relative pose.

B. 4D Radar Inertial Odometry

Compared to 3D radars, 4D imaging radars significantly improve the elevation resolution, though its point clouds are still very sparse (~ 400 points/scan). Meanwhile, the search

space of 4D imaging radar point cloud matching changes from 2D to 3D, and the matching process is affected by various types of noise, thus, it is difficult to achieve stable, continuous, and high-precision scan matching.

To make the odometry more robust and mitigate trajectory drift for missing data and wrong matches in scan-to-scan matching, several works used inertial data as continual observations along with scan-to-scan matching. Almalioglu et al. [16] coupled the radar inter-frame poses obtained from the normal distribution transform and IMU data by an unscented Kalman filter, and used a long short-term memory motion model to estimate 3D ego-motion. Lu et al. [17] proposed a deep neural network based radar inertial odometer, which encoded radar data by a convolutional neural network and IMU data by a recurrent neural network, and achieved real-time pose estimation by a multi-modal sensor fusion network.

Since 4D radar can estimate the 3D ego-velocity from a single scan, many studies coupled IMU measurements with radar single-scan velocity estimates. Kramer et al. [18] proposed a robot velocity estimation method based on sliding window optimization to fuse inertial data with radar ego-velocity, estimating the robot's 3D motion in real time. Doer et al. [19] proposed a radar inertial odometry method based on the extended Kalman filter (EKF) for 3D localization by fusing IMU data with radar ego-velocity estimated by a RANSAC scheme. Moreover, altimeter data were used to eliminate drift in altitude. They [20] further realized online calibration in their system which reduced the localization error nearly twofold. Sequentially, they [5] introduced the Manhattan world assumption as a yaw angle aid for odometry.

Overall, scan matching can give many point constraints, but is sensitive to measurement noise and matching errors [21], and may break down in areas of sparse radar points. The ego-velocity derived from a radar scan is not affected by drift, but is largely unable to correct vertical drift (as shown in Fig. 1). Combining their advantages, we propose a radar inertial odometry method that fuses and single-scan ego-velocity and scan matching which is enhanced by the scan-to-submap concept.

To remedy drift of an odometry method, a loop closure module is needed. For radar-based systems, the current methods for place recognition can be divided into deep learning-based methods, e.g., [22], and traditional geometric methods, e.g., [14], [23]. Learning-based methods can achieve good results for some scenes, but their computation cost and generality is a concern. Thus, we adapt a geometric method, scancontext [23], for loop detection.

III. METHODOLOGY

A. Framework Overview

The proposed iRIOM system is shown in Fig. 2. The inputs are time-aligned radar scans of point clouds and 6D IMU data. To deal with noise points caused by multipath and scattering, we first filter out these points with some spatial statistics in the pre-processing. Second, we propagate the system state (position, attitude, velocity, etc.) by IMU data, estimate the ego-velocity from the incoming radar scan, and obtain point

matches by scan-to-submap matching. The ego-velocity and point matches weighted by their distribution covariances are used to update the system state in an iterated Kalman filter. Third, the radar scan is transformed into the global coordinate system by the estimated pose to update the local submap and the global map. Finally, loops are detected by the scancontext [23]. Loop constraints are computed by the generalized ICP [24] and used in a pose graph optimization along with relative pose constraints, obtaining consistent poses and maps.

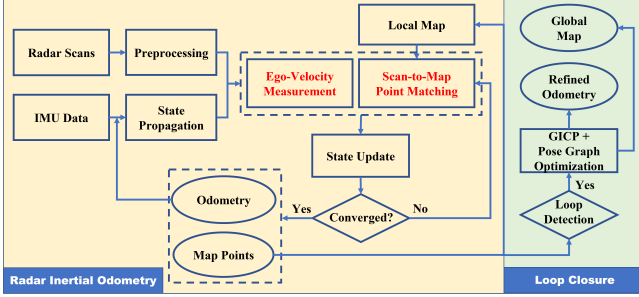


Fig. 2. System overview of iRIOM.

B. Radar Data Preprocessing

Compared to sensors such as lidars and cameras, there is a greater proportion of invalid points in the scans by a radar, including interference points and noise points due to multipath reflections and speckles, which may degrade mapping and positioning. Thus, we pre-process the radar data to remove such points.

In order to achieve an optimal denoising effect while maintaining sufficient radar point observations, we first remove noise points by a relaxation filtering which considers spatial distributions [25]. The rules are defined by

$$\begin{aligned} \mathbf{P} &= \{\mathbf{p}_i | \text{Num}(\mathbf{p}_j) > N_{th} \text{ and } \|\mathbf{p}_i - \mathbf{p}_j\| < D_{th}\} \\ \mathbf{P} &= \{\mathbf{p}_i | \text{Std}(\mathbf{p}_j) < \sigma_{th} \text{ and } \|\mathbf{p}_i - \mathbf{p}_j\| < D_{th}\} \end{aligned} \quad (1)$$

where \mathbf{P} is the set of inlier points, \mathbf{p}_j is a neighboring point of \mathbf{p}_i within the neighborhood radius D_{th} , $\text{Num}(\mathbf{p}_j)$ is the number of neighborhood points, $\text{Std}(\mathbf{p}_j)$ is the statistical standard deviation of the neighboring points, and N_{th} and σ_{th} are their corresponding thresholds.

Points due to moving objects are found in the ego-velocity estimation step. Radar ego-velocity is usually estimated by a least squares method from Doppler velocity observations in a single radar scan [7], [18], [19]. To this end, the iterative methods with variable weights or RANSAC-like methods can be used. However, sparsity of radar point clouds causes the RANSAC-like method to be unstable. Thus, we use the iterative reweighted least squares method to estimate ego-velocity and find moving points. The ideal ego-velocity model is defined as

$$v^d = \boldsymbol{\rho}^T \cdot {}^R\mathbf{v}_m / \|\boldsymbol{\rho}\| \quad (2)$$

where v^d is the Doppler velocity observation, $\boldsymbol{\rho}$ is the position of the radar point in the radar coordinate system, and $\|\boldsymbol{\rho}\|$ is its norm. ${}^R\mathbf{v}_m$ is the radar ego-velocity in the radar coordinate system.

Considering all points in a radar scan, the ego-velocity estimation can be expressed as a robust estimation problem,

$$\min_{{}^R\mathbf{v}_m} \sum_{i=1}^n \lambda_i \|v_i^d - \boldsymbol{\rho}_i^T \cdot {}^R\mathbf{v}_m / \|\boldsymbol{\rho}_i\|\| \quad (3)$$

where λ_i is the weight of the i -th radar point. In the first iteration, $\lambda_i = 1$, and in the subsequent iterations, $\lambda_i = 1/(\|v_i^d - \boldsymbol{\rho}_i^T \cdot {}^R\mathbf{v}_m / \|\boldsymbol{\rho}_i\|\| + \epsilon)$, $\epsilon = 0.00001$.

By using the iterative reweighted least squares method [26], [27], we get the radar ego-velocity ${}^R\mathbf{v}_m$ and its measurement noise covariance \mathbf{R}_{vel} by taking the inverse of the least squares information matrix. Also, the weight λ_i reflects the probability of a radar point belonging to the static environment. Then, we select a weight threshold λ_{th} , and if $\lambda_i < \lambda_{th}$, the point is deemed to be on a moving object. The remaining static points are the input to the subsequent localization and mapping.

C. IMU State Propagation

We denote by \mathbf{x} the state, \mathbf{u} the control input (i.e., IMU data), and \mathbf{w} the system noise,

$$\begin{aligned} \mathbf{x} &= [{}^G\mathbf{p}_I, {}^G\mathbf{v}_I, {}^G\mathbf{R}_I, \mathbf{b}_a, \mathbf{b}_\omega, {}^I\mathbf{R}_R, {}^I\mathbf{l}_R, {}^G\mathbf{g}] \\ \mathbf{u} &= [\mathbf{a}_m, \boldsymbol{\omega}_m] \quad \mathbf{w} = [\mathbf{n}_a, \mathbf{n}_\omega, \mathbf{n}_{ba}, \mathbf{n}_{b\omega}] \end{aligned} \quad (4)$$

where ${}^G\mathbf{p}_I, {}^G\mathbf{v}_I, {}^G\mathbf{R}_I$ are the position, velocity, and attitude of the IMU in the global coordinate system, resp., $\mathbf{b}_a, \mathbf{b}_\omega$ are the accelerometer and gyro biases modeled as a random walk process with Gaussian noise $\mathbf{n}_a, \mathbf{n}_\omega$, and ${}^I\mathbf{R}_R, {}^I\mathbf{l}_R$ are the orientation and position of the radar in the IMU frame. ${}^G\mathbf{g}$ is the gravity vector in the global frame. $\mathbf{a}_m, \boldsymbol{\omega}_m$ are the linear acceleration and angular velocity data with Gaussian process noises of $\mathbf{n}_a, \mathbf{n}_\omega$, resp. The global frame is chosen to be the IMU frame at the start of the SLAM system. Since the global frame's z -axis may not coincide the gravity, the gravity is put in the state and its direction is estimated by the filter.

The discretized propagation model at $\mathbf{x} = \mathbf{x}_i$ with IMU data is given by

$$\begin{aligned} \mathbf{x}_{i+1}(1:3) &\approx \begin{bmatrix} {}^G\mathbf{p}_{I_i} + {}^G\mathbf{v}_{I_i}\Delta t \\ {}^G\mathbf{v}_{I_i} + ({}^G\mathbf{R}_{I_i}(\mathbf{a}_m - \mathbf{b}_{a_i}) + {}^G\mathbf{g}_i)\Delta t \\ {}^G\mathbf{R}_{I_i} \cdot \exp((\boldsymbol{\omega}_m - \mathbf{b}_{\omega_i})\Delta t) \end{bmatrix} \\ \mathbf{x}_{i+1}(4:8) &\approx \mathbf{x}_i(4:8) \end{aligned} \quad (5)$$

where Δt is the IMU sampling interval, and the indices 1:3 refer to the first three variables of \mathbf{x}_{i+1} .

We define the error state as in [28],

$$\tilde{\mathbf{x}} = [{}^G\tilde{\mathbf{p}}_I, {}^G\tilde{\mathbf{v}}_I, {}^G\tilde{\mathbf{R}}_I, \tilde{\mathbf{b}}_a, \tilde{\mathbf{b}}_\omega, {}^I\tilde{\mathbf{R}}_L, {}^I\tilde{\mathbf{l}}_L, {}^G\tilde{\mathbf{g}}]. \quad (6)$$

Propagation of the error state and its covariance $\hat{\mathbf{P}}$ is given by

$$\tilde{\mathbf{x}}_{i+1} = \mathbf{x}_{i+1} \ominus \hat{\mathbf{x}}_{i+1} \approx \mathbf{F}_{\tilde{\mathbf{x}}} \tilde{\mathbf{x}}_i + \mathbf{F}_{\mathbf{w}} \mathbf{w}_i \quad (7)$$

$$\hat{\mathbf{P}}_{i+1} = \mathbf{F}_{\tilde{\mathbf{x}}} \hat{\mathbf{P}}_i \mathbf{F}_{\tilde{\mathbf{x}}}^T + \mathbf{F}_{\mathbf{w}} \mathbf{Q}_{i+1} \mathbf{F}_{\mathbf{w}}^T \quad (8)$$

where $\hat{\mathbf{x}}_{i+1}$ is the state predicted by IMU propagation, \ominus is the state minus operation, in which ${}^G\mathbf{R}_{I_{i+1}} \ominus {}^G\hat{\mathbf{R}}_{I_{i+1}} = \log({}^G\mathbf{R}_{I_{i+1}} {}^G\hat{\mathbf{R}}_{I_{i+1}}^T)$, ${}^I\mathbf{R}_{i+1} \mathbf{R}_{R_{i+1}} \ominus {}^I\mathbf{R}_{i+1} \hat{\mathbf{R}}_{R_{i+1}} =$

$\log(I_{i+1}\mathbf{R}_{R_{i+1}}^{I_{i+1}}\hat{\mathbf{R}}_{R_{i+1}}^T)$, and the others follow the common minus operation.

$$\mathbf{F}_{\tilde{\mathbf{x}}} = \begin{bmatrix} \mathbf{F}_A & \mathbf{F}_B \\ \mathbf{0}_{15 \times 9} & \mathbf{I}_{15 \times 15} \end{bmatrix} \quad (9)$$

$$\mathbf{F}_A = \begin{bmatrix} \mathbf{I} & \mathbf{I}\Delta t & \mathbf{0} \\ \mathbf{0} & \mathbf{I} & \mathbf{F}_v^R \\ \mathbf{0} & \mathbf{0} & \mathbf{F}_R^R \end{bmatrix} \quad \mathbf{F}_B = \begin{bmatrix} \mathbf{0} & \mathbf{0} & \mathbf{0} & \mathbf{0} & \mathbf{0} \\ \mathbf{F}_v^{b_a} & \mathbf{0} & \mathbf{0} & \mathbf{0} & \mathbf{I}\Delta t \\ \mathbf{0} & \mathbf{F}_R^{b_\omega} & \mathbf{0} & \mathbf{0} & \mathbf{0} \end{bmatrix} \quad (10)$$

where $\mathbf{F}_v^R = -^G\mathbf{R}_{I_i}(\mathbf{a}_m)_{\times} \Delta t$, $\mathbf{F}_v^{b_a} = -^G\mathbf{R}_{I_i} \Delta t$, $\mathbf{F}_R^R = \exp(-\omega_m \Delta t)$, $\mathbf{I} = \mathbf{I}_{3 \times 3}$, $\mathbf{F}_R^{b_\omega} = -\mathbf{A}(\omega_m \Delta t)^T \Delta t$ in which $\mathbf{A}(\cdot)^{-1}$ is defined in [28].

D. Ego-Velocity Measurements

The ego-velocity $^R\mathbf{v}_m$ in the radar frame estimated from a radar scan can serve as the velocity measurement,

$$\mathbf{r}_v = ^R\mathbf{v} - ^R\mathbf{v}_m \approx \hat{\mathbf{r}}_v + \mathbf{H}_v \tilde{\mathbf{x}} \quad (11)$$

$$^R\mathbf{v} = ^I\mathbf{R}_R^T (^G\mathbf{R}_I^T \mathbf{v}_I + (\omega_m - \mathbf{b}_\omega)_{\times} ^I\mathbf{l}_R) \quad (12)$$

where $\hat{\mathbf{r}}_v$ is the residual and \mathbf{H}_v is the Jacobian matrix of $\hat{\mathbf{r}}_v$ relative to the error state, as derived in [20].

We prune those 3D ego-velocity measurements with the Mahalanobis distance of $\mathbf{r}_v > \chi_{3,0.05}^2$ value at significance level 0.05. In the update step, the Kalman gain is calculated as

$$\mathbf{K}_v = \mathbf{P}\mathbf{H}_v^T (\mathbf{H}_v\mathbf{P}\mathbf{H}_v^T + \mathbf{R}_v)^{-1} \quad (13)$$

where \mathbf{P} is the covariance of the state \mathbf{x} and \mathbf{R}_v is the measurement covariance matrix. The updated state $\tilde{\mathbf{x}}_v$ and covariance $\tilde{\mathbf{P}}_v$ are

$$\tilde{\mathbf{x}}_v = \hat{\mathbf{x}} \oplus \tilde{\mathbf{x}} = \hat{\mathbf{x}} \oplus (-\mathbf{K}_v \hat{\mathbf{r}}_v) \quad (14)$$

$$\tilde{\mathbf{P}}_v = (\mathbf{I} - \mathbf{K}_v \mathbf{H}_v) \mathbf{P} \quad (15)$$

where \oplus denotes the state plus operation, in which $^G\hat{\mathbf{R}}_{I_{i+1}} \oplus ^G\hat{\mathbf{R}}_{I_{i+1}} = ^G\hat{\mathbf{R}}_{I_{i+1}} \exp(^G\hat{\mathbf{R}}_{I_{i+1}})$, $^{I_{i+1}}\hat{\mathbf{R}}_{R_{i+1}} \oplus ^{I_{i+1}}\hat{\mathbf{R}}_{R_{i+1}} = ^{I_{i+1}}\hat{\mathbf{R}}_{R_{i+1}} \exp(^{I_{i+1}}\hat{\mathbf{R}}_{R_{i+1}})$, and the others follow the common plus operation.

E. Scan-to-Submap Matching Constraints

We also use point cloud matching to achieve higher accuracy for positioning and mapping. Odometry methods based on radar scans usually adopt two types of matching: scan-to-scan or scan-to-submap. Scan-to-scan matching derives point matches from two sequential scans, thus, involves fewer points and relatively lower computation. Otherwise, scan-to-scan matching is less robust and prone to error accumulation with sparse point clouds or substantial changes in local scenes (turning, up-slope, etc.). Scan-to-submap matching maintains a local map to match the current scan. According to the maintenance methods, typical local maps include key-frame sliding window maps based on time sequence updates (GCLO [29], KSWF [30], etc.) and incrementally updated grid maps (ikd-tree [28], iVox [31], etc.). Compared with scan-to-scan matching, scan-to-submap matching has higher stability and accuracy. Thus, we adopt scan-to-submap matching based on the ikd-tree which facilitates real-time computation.

The spatial point matches from scan-to-submap matching are used to update the state in an iterative Kalman filter. The distance of a point match is usually measured by point-to-point, point-to-distribution, or distribution-to-distribution distances [24]. The distribution-to-distribution metric considers the local geometry of the source and the target point to weight the distance residuals. Thus, it is resilient to data noise and suitable for the sparse radar scans.

Due to the sparsity of 4D radar scans, it is difficult to ensure that the points in the current scan and the local map have exact one-to-one matches. Thus, we consider the N nearest neighbor points $^G\mathbf{b}_j$ ($j = 1, \dots, N$, $N = 5$ in our tests) in the submap of a point $^R\mathbf{a}$ in the current scan, weight the distance between $\{^G\mathbf{b}_j\}$'s centroid and $^R\mathbf{a}$ by their covariance to achieve a distribution-to-multi-distribution effect. The weighting scheme empirically improves the registration of a scan to a submap. The weighted point match distance is computed as

$$\mathbf{r}_p = \mathbf{G}_p(\Sigma_j(^G\mathbf{b}_j/N) - ^G\mathbf{T}_R \cdot ^R\mathbf{a}) \approx \hat{\mathbf{r}}_p + \mathbf{H}_p \tilde{\mathbf{x}} \quad (16)$$

$$^G\mathbf{T}_R = ^G\mathbf{T}_I ^I\mathbf{T}_R = \begin{bmatrix} ^G\mathbf{R}_I & ^G\mathbf{l}_I \\ \mathbf{0}_{1 \times 3} & 1 \end{bmatrix} \begin{bmatrix} ^I\mathbf{R}_R & ^I\mathbf{l}_R \\ \mathbf{0}_{1 \times 3} & 1 \end{bmatrix} \quad (17)$$

$$\mathbf{G}_p = \sqrt{(\Sigma_j(\mathbf{C}_j^B/N) + ^G\hat{\mathbf{T}}_R \cdot \mathbf{C}^A \cdot ^G\hat{\mathbf{T}}_R^T)^{-1}} \quad (18)$$

$$\hat{\mathbf{r}}_p = \mathbf{G}_p(\Sigma_j(^G\mathbf{b}_j/N) - ^G\hat{\mathbf{T}}_R \cdot ^R\mathbf{a}) \quad (19)$$

$$\mathbf{H}_p = [\mathbf{G}_p \quad \mathbf{0}_3 \quad \mathbf{H}_p^R \quad \mathbf{0}_3 \quad \mathbf{0}_3 \quad \mathbf{H}_p^{R_e} \quad \mathbf{H}_p^l \quad \mathbf{0}_3] \quad (20)$$

where \mathbf{C}^A and \mathbf{C}_j^B are the spatial covariance of the five points close to $^R\mathbf{a}$ and $^G\mathbf{b}_j$ (including themselves), resp., and \mathbf{G}_p is the weight matrix. $^G\mathbf{T}_R$ is the transformation matrix from radar coordinate system to global coordinate system. $\hat{\mathbf{r}}_p$ and \mathbf{H}_p are the computed residual and the Jacobian matrix relative to the state, in which $\mathbf{H}_p^R = \mathbf{G}_p(^G\mathbf{R}_I(^I\mathbf{R}_R \cdot ^R\mathbf{a} + ^I\mathbf{l}_R))_{\times}$, $\mathbf{H}_p^{R_e} = \mathbf{G}_p(^G\mathbf{R}_I(^I\mathbf{R}_R \cdot ^R\mathbf{a}))_{\times}$, $\mathbf{H}_p^l = -\mathbf{G}_p^G\mathbf{R}_I$.

During the iterative Kalman filtering update, \mathbf{x} should be kept nearly to the initial estimate $\hat{\mathbf{x}}$, namely

$$\mathbf{x} \ominus \hat{\mathbf{x}} = (\hat{\mathbf{x}}^\kappa \oplus \tilde{\mathbf{x}}^\kappa) \ominus \hat{\mathbf{x}} = (\hat{\mathbf{x}}^\kappa \ominus \hat{\mathbf{x}}) + \mathbf{J}^\kappa \tilde{\mathbf{x}}^\kappa \approx \mathbf{0} \quad (21)$$

$$\mathbf{J}^\kappa = \begin{bmatrix} \mathbf{I}_6 & \mathbf{0}_{6 \times 3} & \mathbf{0}_6 & \mathbf{0}_{6 \times 3} & \mathbf{0}_6 \\ \mathbf{0}_{3 \times 6} & \mathbf{J}_1^\kappa & \mathbf{0}_{3 \times 6} & \mathbf{0}_3 & \mathbf{0}_{3 \times 6} \\ \mathbf{0}_6 & \mathbf{0}_{6 \times 3} & \mathbf{I}_6 & \mathbf{0}_{6 \times 3} & \mathbf{0}_6 \\ \mathbf{0}_{3 \times 6} & \mathbf{0}_3 & \mathbf{0}_{3 \times 6} & \mathbf{J}_2^\kappa & \mathbf{0}_{3 \times 6} \\ \mathbf{0}_6 & \mathbf{0}_{6 \times 3} & \mathbf{0}_6 & \mathbf{0}_{6 \times 3} & \mathbf{I}_6 \end{bmatrix} \quad (22)$$

where $\hat{\mathbf{x}}^\kappa$ is the κ th filter update value, $\tilde{\mathbf{x}}^\kappa$ is the corresponding error state, and \mathbf{J}^κ is the linearized Jacobi matrix (at $\tilde{\mathbf{x}}^\kappa = \mathbf{0}$), $\mathbf{J}_1^\kappa = \mathbf{A} (^G\hat{\mathbf{R}}_I^\kappa \ominus ^G\hat{\mathbf{R}}_I)^{-T}$, $\mathbf{J}_2^\kappa = \mathbf{A} (^I\hat{\mathbf{R}}_R^\kappa \ominus ^I\hat{\mathbf{R}}_R)^{-T}$.

Then the update process can be described as a MAP estimation problem as follows

$$\min_{\tilde{\mathbf{x}}^\kappa} \|(\hat{\mathbf{x}}^\kappa \ominus \hat{\mathbf{x}}) + \mathbf{J}^\kappa \tilde{\mathbf{x}}^\kappa\|_{\tilde{\mathbf{P}}^{-1}}^2 + \sum_{j=1}^m \|{}^j\hat{\mathbf{r}}_p^\kappa + {}^j\mathbf{H}_p^\kappa \tilde{\mathbf{x}}^\kappa\|_{{}^j\mathbf{R}_p^{-1}}^2 \quad (23)$$

where $\hat{\mathbf{x}} = \bar{\mathbf{x}}_{vel}$, $\hat{\mathbf{P}} = \bar{\mathbf{P}}_{vel}$ is the state and covariance matrix after ego-velocity update, and ${}^j\mathbf{R}_p^{-1}$ is the noise covariance for the j -th point.

Solving the above problem, we obtain

$$\mathbf{K}_p^\kappa = \mathbf{P}^\kappa (\mathbf{H}_p^\kappa)^T (\mathbf{H}_p^\kappa \mathbf{P}^\kappa (\mathbf{H}_p^\kappa)^T + \mathbf{R}_p)^{-1} \quad (24)$$

$$\hat{\mathbf{x}}^{\kappa+1} = \hat{\mathbf{x}}^{\kappa} \oplus \left(-\mathbf{K}_p^{\kappa} \hat{\mathbf{r}}_p^{\kappa} - (\mathbf{I} - \mathbf{K}_p^{\kappa} \mathbf{H}_p^{\kappa}) (\mathbf{J}^{\kappa})^{-1} (\hat{\mathbf{x}}^{\kappa} \ominus \hat{\mathbf{x}}) \right) \quad (25)$$

where $\mathbf{H}_p^{\kappa} = [\mathbf{H}_p^{\kappa,1}, \mathbf{H}_p^{\kappa,2}, \dots, \mathbf{H}_p^{\kappa,m}]$, $\mathbf{R}_p = \text{diag}(\mathbf{R}_p^1, \mathbf{R}_p^2, \dots, \mathbf{R}_p^m)$, $\mathbf{P}^{\kappa} = (\mathbf{J}^{\kappa})^{-1} \hat{\mathbf{P}} (\mathbf{J}^{\kappa})^{-T}$.

When the iterations converge or reach the maximum iterations, the projection residual optimization state $\bar{\mathbf{x}}_p$ and covariance $\bar{\mathbf{P}}_p$ can be obtained as

$$\bar{\mathbf{x}}_p = \hat{\mathbf{x}}^{\kappa+1} \quad (26)$$

$$\bar{\mathbf{P}}_p = (\mathbf{I} - \mathbf{K}_p^{\kappa} \mathbf{H}_p^{\kappa}) \mathbf{P}^{\kappa} \quad (27)$$

where $\hat{\mathbf{x}}^{\kappa+1}$ is the filter state of the $\kappa + 1$ iteration and \mathbf{K}_p^{κ} is the Kalman gain calculated from the κ iteration.

IV. EXPERIMENTS

A. In-house Data

We equipped a ground robot with a 4D radar ARS548 from Continental, which scans at 15 Hz in the 76 – 77 GHz, with an elevation angle of view (AOV) $\pm 20^\circ$ and an azimuth AOV $\pm 60^\circ$, azimuth angle resolution 0.2° , elevation angle resolution 0.1° , detection range ~ 300 m, and distance accuracy 0.3 m. The reference trajectory is obtained by the Bynav X1-5H GNSS/INS module in open sky areas. The data from the Bynav module's built-in IMU (EPSON G345) are fused with the radar data. The IMU has a gyroscope bias stability $0.00075^\circ/\text{s}$, angular random walk $0.003^\circ/\sqrt{\text{s}}$, accelerometer bias stability $70 \mu\text{g}$, and the velocity random walk $0.0005 \text{ m}/\sqrt{\text{s}^3}$. The robot and sensors are shown in Fig. 3.

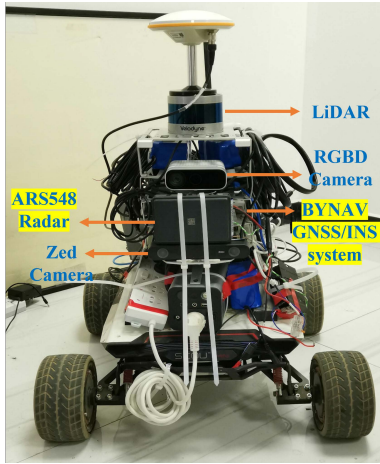


Fig. 3. The ground robot and the sensors for tests. Note that the ZED camera and the RGBD camera are not used.

We collected data in two outdoor scenes and one indoor scene. We began the data collection at an area with open sky and performed maneuvers of straight lines and then figure eight curves to make sure the GNSS RTK and the INS system is well aligned, so that we have accurate reference. The reported accuracy of the Bynav module is ~ 3 cm with profuse RTK data, but drops to 25 cm with a 10-second RTK outage.

Sequence 1 is at an outdoor basketball court surrounded by trees. The 6-minute data has a maximum velocity 3 m/s

TABLE I
STATISTICS OF EKFRIO, iRIO, AND iRIOM ON OUR SEQUENCE 1-3

	Method	Closure Error		APE RMSE		RPE RMSE	
		Hor	Ver	Trans	Rot	Trans	Rot
1	EKFRIO	0.530	15.759	5.616	10.261	0.055	0.183
	iRIO	0.029	0.010	0.313	2.923	0.040	0.171
	iRIOM	0.027	0.010	0.305	2.751	0.040	0.171
	FastLIO	0.024	0.007	0.147	5.331	0.025	0.343
2	EKFRIO	17.194	24.631	10.068	9.859	0.026	0.120
	iRIO	1.517	5.073	1.518	2.866	0.022	0.114
	iRIOM	0.279	0.001	0.336	2.626	0.022	0.112
	FastLIO	0.151	0.025	0.372	6.363	0.020	0.322
3	EKFRIO	3.741	9.268	3.388	8.655	0.183	0.458
	iRIO	0.051	0.032	0.303	8.368	0.132	0.343
	iRIOM	0.050	0.032	0.307	8.359	0.131	0.340
	FastLIO	0.012	0.007	—	—	—	—

^a APE Rot. RMSEs are in $^\circ$, APE Trans. RMSEs and Closure Errors are in m. RPE Rot. RMSEs are in $^\circ/\text{m}$, and RPE Trans. RMSEs are in %.

^b FastLIO denotes FastLIO-SLAM. GNSS/INS results was unreliable for sequence 3, so we took the FASTLIO-SLAM trajectory as reference. Thus, the RMSEs of FastLIO-SLAM on sequence 3 are zero.

and large angular velocity at turns. The whole session has the centimeter-level GNSS RTK/INS solution as the reference, and we also started and stopped at the same pose.

Sequence 2 is collected traversing around the Xinghu Building in Wuhan University for two laps. There are numerous vehicles, pedestrians, and other moving targets. The 9-minute data has a maximum speed about 2 m/s and angular speed at turns is small. Despite occasional short GNSS blockages due to high-rises, the INS poses were always reported good, and the trajectory started and stopped at the same pose.

Sequence 3 is an underground parking lot with narrow passageways and serious occlusions. The ground and walls in the scene are very smooth, leading to multipath reflections and a large number of “ghost” points. The 5-minute data has a maximum speed 2 m/s and small angular speed at turns. The GNSS/INS solution was somewhat unreliable, but the trajectory started and stopped at the same pose.

B. In-house Data Results

For all three sequences, we evaluate the algorithm performance by the trajectory closure error (CE). To mitigate randomness, we run an algorithm 10 times on each sequence and calculated the mean value of the closure error. Moreover, we evaluate the accuracy of the methods by calculating the difference of the estimated trajectory to the reference. For sequence 1 and 2, we take the centimeter-level trajectory obtained by the fusion of GNSS and IMU as reference, and evaluate the pose estimation accuracy by calculating the root mean square error (RMSE) between the reference trajectory and the algorithm results, include the absolute pose error (APE) and the relative pose error (RPE). For sequence 3, we obtain a rough reference trajectory by fusing lidar and IMU data by FastLIO-SLAM [28].

We conduct comparison with the EKFRIO method in [20] and a recent lidar SLAM method, FastLIO-SLAM [28]. EKFRIO is the best-performing open-source 4D radar inertial

odometry method known to us. Lidar data for FastLIO-SLAM was obtained from the Velodyne VLP-16 on the robot. We tested two variants of iRIOM: the iRIO without loop closure and the iRIOM. The accuracy statistics on our three sequences are shown in Table I. We see that the position accuracy of iRIO is much better than that of EKFRIO, and iRIOM further reduces the drift in the Z-direction by loop closure. Also, the accuracy of iRIOM is comparable to that of FastLIO-SLAM on these sequences.

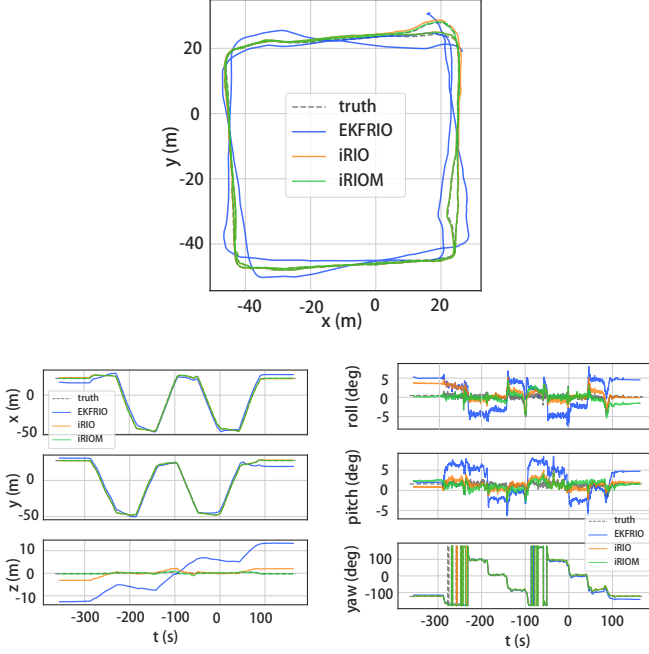


Fig. 4. Top: Trajectories estimated by the EKFRIO, iRIO and iRIOM on our sequence 2. Bottom: The position and attitude of estimated trajectories by these methods aligned to the reference.

For sequence 2, Fig. 4 shows the trajectories estimated by the three radar methods along with the ground truth. Fig. 5 shows the trajectory closure error of iRIO on sequence 2. Both figures show that by using scan-to-submap point matching, the trajectory closure error and trajectory RMSEs of iRIO are significantly lower than those of EKFRIO. However, due to the large scene of sequence 2, iRIO still has a large drift in the Z-direction. The iRIOM method further refines the position and attitude results by loop closure, thus, the trajectory closure error is reduced by an order of magnitude.

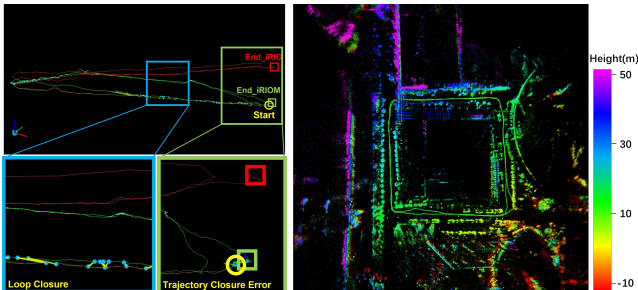


Fig. 5. The detected loop closure and closure error (left), and the mapping result of iRIOM (right) on our sequence 2 where points are colored by height.

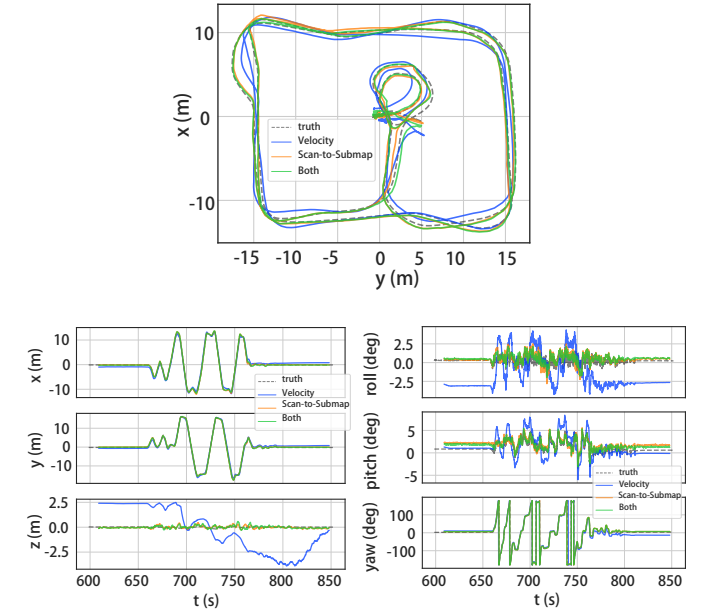


Fig. 6. Top: Trajectories of variants of iRIOM described in Section IV-C on our sequence 1. Velocity: Only using ego-velocity for filter update; Scan-to-submap: only using scan-to-submap matches for filter update; Both: both measurements are used for update. Bottom: The position and attitude of estimated trajectories by these variants aligned to the reference.

TABLE II
TIMING STATISTICS(MAX/MIN AND MEAN IN MS) OF IRIOM ON OUR SEQUENCE 1-3

	IMU predict	Ego vel. update	Scan-to-Submap update	Total
1	10.66 / 0.09 0.24	13.42 / 0.05 0.47	379.18 / 1.47 48.69	380.08 / 1.72 49.41
2	9.53 / 0.08 0.19	6.24 / 0.06 0.51	284.55 / 2.28 50.07	285.10 / 3.13 50.77
3	4.89 / 0.08 0.18	2.84 / 0.05 0.36	119.29 / 0.34 12.87	120.55 / 0.75 13.41

We also calculated the running time of our algorithm shown in Table II. The iRIOM method can run in real time on a consumer laptop processing our ARS548 dataset with ~ 15 Hz radar scans. The most costly part of iRIOM is the scan-to-submap matching which includes the iterative EKF update. The running times are also related to the scene as iRIOM runs much faster indoors than outdoors. We believe this is caused by the submap maintenance.

C. Ablation Studies

To verify the effect of the IMU data, ego-velocity constraints, scan-to-submap matching constraints, we tested ablated variants of iRIOM on our three sequences. The benefit of the IMU data is validated against a constant velocity model for prediction. We also compare the scan-to-submap matching with a temporal scan-to-scan matching. Note that we disable the loop closure module to highlight the effect of each type of constraints.

For variants of iRIOM, Table III lists the trajectory closure errors and trajectory RMSEs. Fig. 6 shows the trajectory

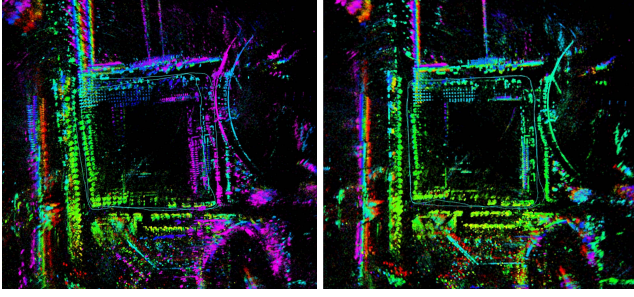


Fig. 7. The mapping results of iRIO with scan-to-five-scans matching and with the default scan-to-submap matching.

estimation results of the ablated iRIOM with either the ego-velocity or the scan-to-submap matches on our sequence 1. Also shown in Fig. 1, quantitatively, the mapping results with only ego-velocity constraints still have apparent blur and vertical drift. The point matches helped better estimate the map points and significantly reduce the mapping blur. Fig. 7 shows the mapping results of the iRIO variant with scan-to-five-scans matching.

TABLE III
ABLATION TEST STATISTICS ON OUR SEQUENCE 1-3

Meas.	F	Closure Error		RMSE APE		RMSE RPE		
		Hor	Ver	Trans	Rot	Trans	Rot	
1	Vel.	1	2.398	2.606	2.327	9.744	0.046	0.229
	S2M	4	0.023	0.091	0.342	2.926	0.042	0.172
	Both	0	0.029	0.010	0.313	2.923	0.040	0.171
	CVM	5	25.598	1.433	9.106	8.591	0.121	0.300
	S2S	2	3.402	1.314	1.441	5.398	0.043	0.277
2	Vel.	1	25.422	8.913	3.367	13.298	0.022	0.172
	S2M	1	1.540	5.417	1.556	2.981	0.023	0.172
	Both	0	1.517	5.073	1.518	2.866	0.022	0.114
	CVM	3	5.875	9.697	4.611	3.720	0.040	0.238
	S2S	2	8.372	15.599	5.403	6.728	0.033	0.262
3	Vel.	0	2.093	5.436	2.709	11.807	0.177	0.401
	S2M	3	0.368	0.225	0.468	8.769	0.149	0.343
	Both	0	0.051	0.032	0.303	8.368	0.132	0.343
	CVM	3	6.183	9.613	4.049	12.607	0.198	0.639
	S2S	1	3.689	1.482	2.067	10.694	0.168	0.531

^a Vel.: radar ego-velocity constraint, S2M: scan-to-submap matching, Both: Vel. and S2M, CVM: constant velocity model for state prediction, S2S: scan-to-five-scans matching.

^b F means the number of failures in 10 repetitions.

^c APE Rot. RMSEs are in $^{\circ}$, APE Trans. RMSEs and Closure Errors are in m. RPE Rot. RMSEs are in $^{\circ}/m$, and RPE Trans. RMSEs are in $\%$.

From Table III, we see that:

(1) Closure errors of the three sequences are large when only ego-velocity constraints are used, especially in the Z-direction, and the APE RMSE in position exceeds 2 m.

(2) When only scan-to-submap matching is used, estimation failure occurs frequently because of match failures or incorrect matches. However, in successful operations, the location accuracy is relatively high and the trajectory closure error is small. This shows that scan-to-submap matching can mitigate the trajectory drift in the Z-direction especially for small scenes (sequence 1 and 3).

(3) When the velocity constraints and scan-to-submap matching are both used, no estimation failure occurs in the

repeated runs of the three sequences. The mean closure errors and RMSEs of the trajectories are also largely reduced.

(4) When using the constant velocity model for state prediction, the localization accuracy of the system obviously drops. Empirically, more than 3 out of 10 times, the algorithm failed to estimate the trajectory completely without IMU data, and it often deviated from the real trajectory severely midway.

(5) When the size of the temporal window for scan matching is one, i.e., the exact scan-to-scan method, the algorithm stopped working midway in all repeated runs, and the trajectory estimation failed. When the temporal window for scan matching has 5 scans, the algorithm performance significantly improved. However, since this scan-to-five-scan matching only considered the temporally aggregated points instead of all the local points, the algorithm accuracy was still lower than that of the scan-to-submap matching used in iRIOM. Continuing to enlarge the temporal window size greatly increased the computation cost and its benefit on accuracy flattened out.

D. ColoRadar Dataset Results

TABLE IV
STATISTICS OF EKFRIO, iRIO, AND iRIOM ON COLORADAR

	Method	Closure Error		APE RMSE	
		Hor (m)	Vert (m)	Trans (m)	Rot ($^{\circ}$)
Seq 1	EKFRIO	15.732	6.746	5.048	10.758
	iRIO	7.309	0.652	2.377	7.896
	iRIOM	0.351	0.043	0.916	7.198
Seq 2	EKFRIO	0.619	8.045	2.353	12.795
	iRIO	1.254	0.909	0.610	9.050
	iRIOM	0.185	0.195	0.385	8.222

^a Seq 1: 2_23_2021_edgar_classroom_run0.

Seq 2: 2_28_2021_outdoors_run0.

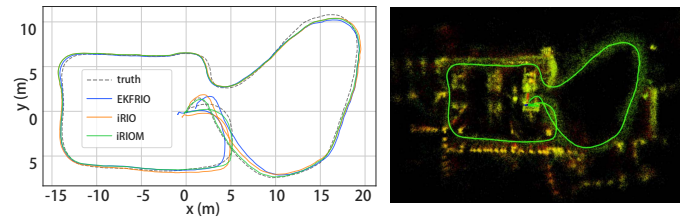


Fig. 8. Left: Trajectory estimated by EKFRIO, iRIO, and iRIOM on 2_28_2021_outdoors_run0 sequence. Right: The mapping result of iRIOM.

To verify the generality of our algorithm, we ran experiments on the ColoRadar sequences [6]. As shown in Table IV and Fig. 8, the experimental results on indoor (2_23_2021_edgar_classroom_run0) and outdoor (2_28_2021_outdoors_run0) sequences indicate that proposed algorithm has good generality while achieving high accuracy localization and mapping.

V. CONCLUSIONS

This paper presents a 4D radar inertial odometry and mapping method, iRIOM, in 3D space, which fuses IMU data, ego-velocity from a radar point cloud scan, and point matches

from scan-to-submap matching. The radar velocity relative to the static world is estimated by a iterative reweighted least squares method, addressing moving objects and multipath effects. Scan-to-submap matching leverages the accumulative points in a local area, and the point matches are weighted by a distribution-to-multi-distribution scheme to deal with non-exact point matching. Experimental results showed that our method achieved accurate odometry and consistent mapping wrt. EKFVIO and FastLIO-SLAM on our and ColoRadar dataset. Ablation study validated the benefits of IMU data, scan-to-submap matching, and loop closure. To our knowledge, iRIOM is the first to achieve real-time 3D odometry and consistent mapping using 4D radar data.

In the future, we would like to explore other constraints, such as the Manhattan world assumption [5] and ground planes [29], and integrate other sensor modalities, e.g., cameras [30].

SUPPLEMENTARY MATERIAL

A video showing iRIOM on our and ColoRadar sequences is at <https://youtu.be/FI9CbSmbd8M>.

ACKNOWLEDGMENTS

We thank the topical editor and anonymous reviewers for their helpful and inspiring comments. Also, downloading the ColoRadar dataset by Yuxin Shao is deeply appreciated.

REFERENCES

- [1] J. Dickmann, J. Klappstein, M. Hahn, N. Appenrodt, H.-L. Bloecher, K. Werber, and A. Sailer, "Automotive radar the key technology for autonomous driving: From detection and ranging to environmental understanding," in *2016 IEEE Radar Conference (RadarConf)*. Philadelphia, PA, USA: IEEE, 2016, pp. 1–6.
- [2] G. Brooker, M. Bishop, and S. Scheding, "Millimetre waves for robotics," in *Australian Conference for Robotics and Automation*, 2001.
- [3] D. Kellner, M. Barjenbruch, J. Klappstein, J. Dickmann, and K. Dietmayer, "Instantaneous ego-motion estimation using Doppler radar," in *16th IEEE Int. Conf. on Intelligent Transportation Systems (ITSC 2013)*. IEEE, 2013, pp. 869–874.
- [4] S. Sun and Y. D. Zhang, "4d automotive radar sensing for autonomous vehicles: A sparsity-oriented approach," *IEEE Journal of Selected Topics in Signal Processing*, vol. 15, no. 4, pp. 879–891, 2021.
- [5] C. Doer and G. F. Trommer, "Yaw aided radar inertial odometry using manhattan world assumptions," in *2021 28th Saint Petersburg Int. Conf. on Integrated Navigation Systems (ICINS)*. St. Petersburg, Russia: IEEE, 2021, pp. 1–9.
- [6] A. Kramer, K. Harlow, C. Williams, and C. Heckman, "Coloradar: The direct 3D millimeter wave radar dataset," *The International Journal of Robotics Research*, vol. 41, no. 4, pp. 351–360, 2022.
- [7] J. Michalczyk, R. Jung, and S. Weiss, "Tightly-coupled EKF-based radar-inertial odometry," in *2022 IEEE/RSJ International Conference on Intelligent Robots and Systems (IROS)*. Kyoto, Japan: IEEE, 2022, pp. 12 336–12 343.
- [8] S. H. Cen and P. Newman, "Precise ego-motion estimation with millimeter-wave radar under diverse and challenging conditions," in *2018 IEEE Int. Conf. on Robotics and Automation (ICRA)*. Brisbane, Australia: IEEE, 2018, pp. 6045–6052.
- [9] —, "Radar-only ego-motion estimation in difficult settings via graph matching," in *2019 Int. Conf. on Robotics and Automation (ICRA)*. Montreal, QC, Canada: IEEE, 2019, pp. 298–304.
- [10] R. Aldera, D. De Martini, M. Gadd, and P. Newman, "Fast radar motion estimation with a learnt focus of attention using weak supervision," in *2019 Int. Conf. on Robotics and Automation (ICRA)*. Montreal, QC, Canada: IEEE, 2019, pp. 1190–1196.
- [11] D. Barnes and I. Posner, "Under the radar: Learning to predict robust keypoints for odometry estimation and metric localisation in radar," in *2020 IEEE Int. Conf. on Robotics and Automation (ICRA)*. Virtual: IEEE, 2020, pp. 9484–9490.
- [12] Z. Hong, Y. Petillot, and S. Wang, "Radarslam: Radar based large-scale SLAM in all weathers," in *2020 IEEE/RSJ Int. Conf. on Intelligent Robots and Systems (IROS)*. Las Vegas, USA: IEEE, 2020, pp. 5164–5170.
- [13] K. Burnett, A. P. Schoellig, and T. D. Barfoot, "Do we need to compensate for motion distortion and doppler effects in spinning radar navigation?" *IEEE Robotics and Automation Letters*, vol. 6, no. 2, pp. 771–778, 2021.
- [14] Y. S. Park, Y.-S. Shin, and A. Kim, "Pharao: Direct radar odometry using phase correlation," in *2020 IEEE Int. Conf. on Robotics and Automation (ICRA)*. Virtual: IEEE, 2020, pp. 2617–2623.
- [15] D. Barnes, R. Weston, and I. Posner, "Masking by moving: Learning distraction-free radar odometry from pose information," *arXiv preprint arXiv:1909.03752*, 2019.
- [16] Y. Almalioglu, M. Turan, C. X. Lu, N. Trigoni, and A. Markham, "Millirio: Ego-motion estimation with low-cost millimetre-wave radar," *IEEE Sensors Journal*, vol. 21, no. 3, pp. 3314–3323, 2020.
- [17] C. X. Lu, M. R. U. Saputra, P. Zhao, Y. Almalioglu, P. P. De Gusmao, C. Chen, K. Sun, N. Trigoni, and A. Markham, "Milliego: Single-chip mmwave radar aided egomotion estimation via deep sensor fusion," in *Proceedings of the 18th Conference on Embedded Networked Sensor Systems*, 2020, pp. 109–122.
- [18] A. Kramer, C. Stahoviak, A. Santamaria-Navarro, A.-A. Agha-Mohammadi, and C. Heckman, "Radar-inertial ego-velocity estimation for visually degraded environments," in *2020 IEEE Int. Conf. on Robotics and Automation (ICRA)*. Virtual: IEEE, 2020, pp. 5739–5746.
- [19] C. Doer and G. F. Trommer, "An EKF based approach to radar inertial odometry," in *2020 IEEE Int. Conf. on Multisensor Fusion and Integration for Intelligent Systems (MFI)*. Karlsruhe, Germany: IEEE, 2020, pp. 152–159.
- [20] —, "Radar inertial odometry with online calibration," in *2020 European Navigation Conference (ENC)*. Dresden, Germany: IEEE, 2020, pp. 1–10.
- [21] Q. Li, J. Huai, D. Chen, and Y. Zhuang, "Real-time robot localization based on 2D lidar scan-to-submap matching," in *China Satellite Navigation Conference (CSNC 2021) Proceedings*. Beijing, China: Springer, 2021, pp. 414–423.
- [22] W. Wang, P. P. de Gusmao, B. Yang, A. Markham, and N. Trigoni, "Radarloc: Learning to relocalize in FMCW radar," in *2021 IEEE Int. Conf. on Robotics and Automation (ICRA)*. Xi'an, China: IEEE, 2021, pp. 5809–5815.
- [23] G. Kim and A. Kim, "Scan context: Egocentric spatial descriptor for place recognition within 3D point cloud map," in *2018 IEEE/RSJ Int. Conf. on Intelligent Robots and Systems (IROS)*. Madrid, Spain: IEEE, 2018, pp. 4802–4809.
- [24] K. Koide, M. Yokozuka, S. Oishi, and A. Banno, "Voxelized GICP for fast and accurate 3D point cloud registration," in *2021 IEEE Int. Conf. on Robotics and Automation (ICRA)*. Xi'an, China: IEEE, 2021, pp. 11 054–11 059.
- [25] H. Balta, J. Velagic, W. Bosschaerts, G. De Cubber, and B. Siciliano, "Fast statistical outlier removal based method for large 3D point clouds of outdoor environments," *IFAC-PapersOnLine*, vol. 51, no. 22, pp. 348–353, 2018.
- [26] P. W. Holland and R. E. Welsch, "Robust regression using iteratively reweighted least-squares," *Communications in Statistics-theory and Methods*, vol. 6, no. 9, pp. 813–827, 1977.
- [27] J. Li, "A practical $O(N^2)$ outlier removal method for correspondence-based point cloud registration," *IEEE Transactions on Pattern Analysis and Machine Intelligence*, vol. 44, no. 8, pp. 3926–3939, 2021.
- [28] W. Xu, Y. Cai, D. He, J. Lin, and F. Zhang, "Fast-LIO2: Fast direct lidar-inertial odometry," *IEEE Transactions on Robotics*, 2022.
- [29] X. Wei, J. Lv, J. Sun, E. Dong, and S. Pu, "GcIo: Ground constrained lidar odometry with low-drifts for GPS-denied indoor environments," in *2022 Int. Conf. on Robotics and Automation (ICRA)*. Philadelphia PA, USA: IEEE, 2022, pp. 2229–2235.
- [30] J. Huai, Y. Lin, Y. Zhuang, C. K. Toth, and D. Chen, "Observability analysis and keyframe-based filtering for visual inertial odometry with full self-calibration," *IEEE Transactions on Robotics*, vol. 38, no. 5, pp. 3219–3237, 2022.
- [31] C. Bai, T. Xiao, Y. Chen, H. Wang, F. Zhang, and X. Gao, "Faster-LIO: Lightweight tightly coupled lidar-inertial odometry using parallel sparse incremental voxels," *IEEE Robotics and Automation Letters*, vol. 7, no. 2, pp. 4861–4868, 2022.